Journal of Magnetism and Magnetic Materials 401 (2016) 890–896

Contents lists available at ScienceDirect

Journal of Magnetism and Magnetic Materials

journal homepage: www.elsevier.com/locate/jmmm

Thermally activated processes and superparamagnetism in $Bi_{12}MnO_{20}$ nanoparticles: A comparative study

L.A.S. de Oliveira [a,*], A. Pentón-Madrigal [b], A.P. Guimarães [c], J.P. Sinnecker [c]

[a] NUMPEX – Núcleo Multidisciplinar de Pesquisas, Universidade Federal do Rio de Janeiro, Est. de Xerém 27, 25245-390 Duque de Caxias, RJ, Brazil
[b] Facultad de Física, Universidad de La Habana, San Lazaro y L, C. Habana CP 10400, Cuba
[c] Centro Brasileiro de Pesquisas Físicas, Rua Xavier Sigaud 150, 22290-180 Rio de Janeiro, RJ, Brazil

ARTICLE INFO

Article history:
Received 24 March 2015
Received in revised form
16 October 2015
Accepted 2 November 2015
Available online 9 November 2015

Keywords:
Fine-particle systems
Temperature-hysteresis effect
Relaxation effect

ABSTRACT

Manganese sillenite ($Bi_{12}MnO_{20}$) nanoparticles having average particle size between 22 and 43 nm were synthesized by a low temperature soft chemical route under refluxing conditions. A careful structural and microstructural characterization by means of high resolution X-ray diffraction experiments and transmission electron microscopy is presented. The as-cast powder displayed an isotropic superparamagnetic (SPM) behavior with a blocked state for temperatures below $T_B \sim 13.0$ K. We used three different measurement techniques to extract and compare the $Bi_{12}MnO_{20}$ blocking temperatures. First, we extracted T_B with the modified Bean–Livingstone model from the coercive field temperature dependence obtained from hysteresis curves measured as a function of temperature. Then, the blocking temperature distribution function, $f(T_B)$, was obtained by deriving the zero field-cooled/field-cooled curves difference. For each applied field, the maximum of the distribution function gave us the mean blocking temperature value. Finally, the maximum of the magnetic susceptibility imaginary part as a function of frequency was used, combined with the Néel–Brown equation, to extract the blocking temperature. All measurement techniques yield an equivalent dependence of T_B with H of the $Bi_{12}MnO_{20}$ superparamagnetic nanoparticles.

1. Introduction

The continuous development of nanoparticle science and technology still opens exciting opportunities for the design of microelectronic devices. In particular, the sillenites are classified as one important material family on this field. Sillenites exhibit a vast variety of physical properties; they can be used as piezoelectric, insulating, photoconductors, photoluminescent, electro-optical and magneto-optical materials. The bismuth oxide, Bi_2O_3, has a wide polymorphism [1], namely α-monoclinic, β-tetragonal, γ-body-centered cubic (BCC) and δ-face-centered cubic (FCC). From all these different phases, the γ-phase BCC with space group I23 and a $\sim$ 10 Å has emerged as being of particular interest in both fundamental aspects and technological applications [2–6].

This structure, known as sillenite, is a metastable phase for pure bismuth oxide, however it can be stabilized by the presence of small amounts of other cations, such as Si, Ge, Ti, Ga, Mn, etc. Generally, stoichiometric sillenite has a formula $Bi_{12}MO_{20}$, where M denotes the cation of an added oxide or a combination of appropriate oxides. The former compound crystallizes into a deformed polyhedra structure consisting of Bi–O (where the Bi ions are coordinated to five oxygen ions) and MO_4 tetrahedra placed in the center and vertices of the unit cell [7].

Preliminary magnetic and structural characterization of polycrystalline $Bi_{12}MnO_{20}$ (BMO) obtained by a simple procedure [8] has shown a classical nanoparticle behavior. According to X-ray diffraction experiments, particle size around 30–40 nm have been obtained. However, a detailed study of the magnetic properties yields a magnetic dynamic behavior of this nanoparticle system following an Arrhenius law with unusual relaxation time [8]. In the presence of an external DC field, the usual relaxation time, of the order of 10^{-9}, was recovered. This result suggests the possibility of having a non-homogeneous nanoparticle size distribution with even smaller dimensions than those obtained from X-ray diffraction experiments previously reported.

In the present work a careful structural and microstructural characterization by means of high resolution X-ray diffraction experiments and transmission electron microscopy is presented, as well as a complete and comparative study of the thermal activated processes in order to clarify the nanoparticle's behavior previously reported.

* Corresponding author.
E-mail address: laso@xerem.ufrj.br.br (L.A.S. de Oliveira).

http://dx.doi.org/10.1016/j.jmmm.2015.11.013
0304-8853/

2. Synthesis and experimental procedure

$Bi_{12}MnO_{20}$ powder samples were prepared using a chemical route based on bismuth oxide (Bi_2O_3), manganese chloride, $MnCl_2 \cdot 4H_2O$, sodium hydroxide (NaOH), and hydrochloride acid (HCl) as described elsewhere [1]. The final solution obtained was continuously stirred for times between 6 and 8 h in an oil bath with temperature around 393 K. Once the precipitates were obtained, they were filtered and washed with distilled water, and oven dried for 12 h at 373 K. Finally, the sample was grounded into a fine powder in an agate mortar. A first sample, referred here as 04B1, was synthesized with excess Bi_2O_3 (to compensate for Bi losses) and with 6 h digest. A second one, referred here as 08A1, was synthesized with an equimolar concentration of the precursors, using an 8 h digest. High resolution X-ray diffraction experiments (XRD) were conducted on the XRD beamline at the Brazilian Synchrotron Light Source facility (LNLS). The Bragg–Brentano optical system consisted of a bending magnet light source, a double-crystal Si (111) monochromator and a Ge (111) crystal analyzer. The specimen was mounted in a 10 mm diameter rotating sample holder and the radiation energy was set to 10 keV, which corresponds to a wavelength of 1.238840 Å. The powder diffraction data were collected at room temperature, with a step of 0.02°, at fixed number of counts. A LaB_6 sample was used as an external standard reference material (SRM), in order to remove any instrumental contribution to the diffraction profiles. High resolution transmission electron microscopy (HRTEM) was conducted with a JEOL 3010 (300 kV with LaB_6 filament) at the Brazilian Nanotechnology National Laboratory (LNNano) facility. Magnetic measurements were performed either in a Quantum Design Physical Property Measurement System (PPMS - 9T), or in a Cryogenics SQUID magnetometer.

3. Results and discussion

3.1. Structure

Fig. 1 shows the X-ray diffraction pattern of the 04B1 and 08A1 samples. The patterns can be indexed to a BMO phase with a BCC crystal structure, belonging to the I23 space group and cell constant values of $a = 10.176(1)$ Å and $a = 10.163(2)$ Å for 04B1 and 08A1, respectively, consistent with the reported data ICSD # 75079. In both cases well-crystallized BMO crystallites could be easily achieved by the present refluxing process. In the case of the 08A1 sample, small traces of a spurious unknown phase were also observed (marked with arrows).

The diffraction patterns were fitted using a profile matching mode [9] implemented in the Fullprof program [10]. At the bottom of the main diffraction peaks an appreciable increase of the background is observed, particularly for the sample 08A1, as shown by the background baseline in Fig. 2.

This background can be related either to an amorphous component in the sample or to the presence of a smaller particle size distribution, and it cannot be fitted with a sixth-order polynomial, as implemented in Fullprof code [10]. Therefore, an automatic background point selection was performed and used during the refinement procedure. In Fig. 1 the points represent the experimental data, the solid curve the fitted pattern, the vertical bars the calculated Bragg positions and the curve at the bottom, the difference between experimental and calculated patterns. The values of Rwp in each case are slightly above 10%, due to the background and the presence of the second phase.

An X-ray line profile analysis using the classical Williamson–Hall (WH) method [11] for deconvoluting size and strain contributions to line broadening, as a function of 2θ, is shown in Fig. 3.

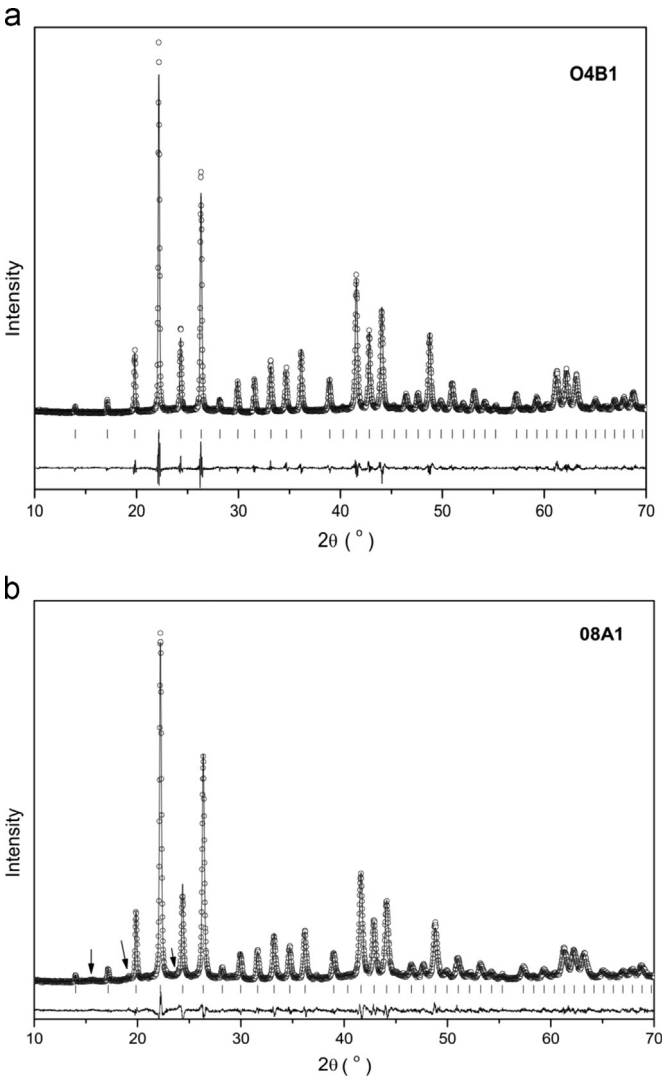

Fig. 1. X-ray diffraction patterns of the (a) 04B1 and (b) 08A1 samples.

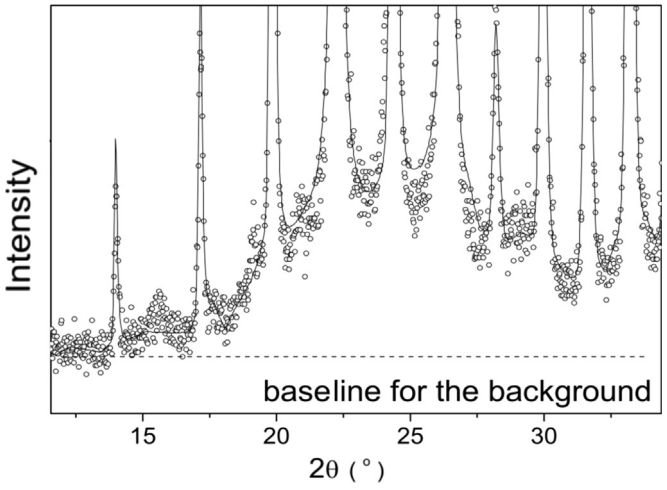

Fig. 2. Detail of the X-ray diffraction profile of sample 08A1, showing the baseline.

In the WH plot, the y-intercept can be used to calculate the average crystallite size, while non-homogeneous microstrain can be calculated from the slope of Fig. 3. The sample 08A1 shows the smallest crystallite size (22 nm) while its microstrain value is slightly higher, a fact that can be related to the decrease in the size

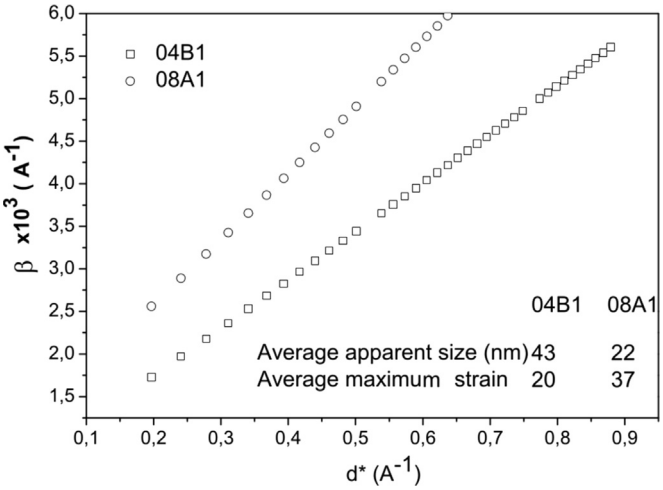

Fig. 3. Williamson Hall plot obtained for samples 04B1 and 08A1.

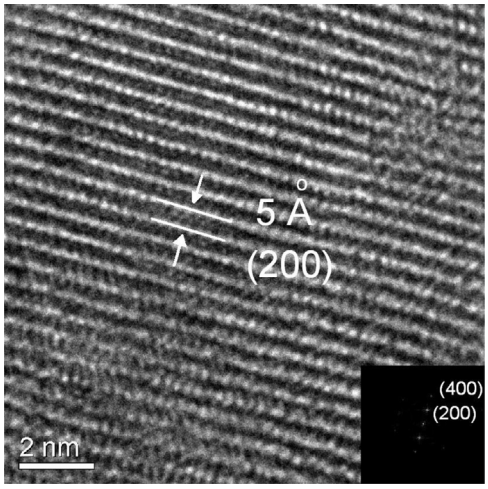

Fig. 5. Detail of a high resolution transmission electron microscopy of an elongated particle from sample 08A1, and its Fast Fourier Transform (inset).

of crystallites.

Fig. 4 shows a low magnification HRTEM micrograph of the sample 08A1 with a distribution of nanometer particles with different morphologies. In Fig. 4a spherical clusters of about 90 nm and an elongated nanoparticle, with cross section of 20 nm and length of 90 nm, are observed. Elongated nanoparticles are also observed in the micrographs of other sample regions with almost the same cross section but with different lengths, ranging from 90 to 120 nm. It is worth noticing that this elongated heterostructure exhibits a systematic border contrast in comparison with the spherical ones. The proportion of spherical clusters to elongated nanoparticles favors the first significantly. That is why we have not observed any anisotropy in the observed diffraction profiles due to the anisotropic shape of the elongated particles. As a result of the former consideration, the microstructural analysis presented in Fig. 3 is based on the isotropic case, where spherical particle morphology and isotropic non-uniform microstrain are assumed. A high resolution micrograph shows a more detailed view of the area marked in the previous micrograph, revealing crystalline regions within the clusters. These crystalline regions have dimensions of 5–10 nm approximately (Fig. 4b). This particle size distribution is responsible for the observed increased background at the bottom of the most intense diffraction peaks.

Fig. 5 shows a HRTEM of a region within the elongated nanoparticles. Crystallographic planes within the particle with interplanar distance of 5 Å, corresponding to the (200) crystallographic planes were identified. The Fast Fourier Transform (FFT) of this region is shown in the inset of this figure with the reflections (200) and (400), corresponding to interplanar distances of 5 Å and 2.5 Å, respectively. It is in agreement with the calculated values ($d(200)=5.08$ Å and $d(400)=2.54$ Å) from the XRD pattern of this sample.

From the structural analysis we conclude that we are dealing with a nanoparticle system showing an inhomogeneous distribution of particles sizes. The sample 04B1 exhibits an average particle size of 43 nm, while in the sample 08A1 the distribution ranges from 5 to about 22 nm with a minor fraction of particles exhibiting an elongated morphology.

3.2. Comparative study of the thermal activated processes

3.2.1. Blocking temperature from the magnetization loops

Below a certain critical size, the lowest energy configuration for magnetic nanoparticles is a monodomain state [12–14]. In such small particles, the magnetic behavior strongly depends on the time scale (τ_m) of the employed experimental technique with respect to the intrinsic system relaxation time (τ), associated to the energy barrier (ΔE) [15,16]. This measuring time can vary from macroscopic techniques, as in conventional magnetization measurements ($\tau_m=100$ s), to microscopic ones, as in Mössbauer

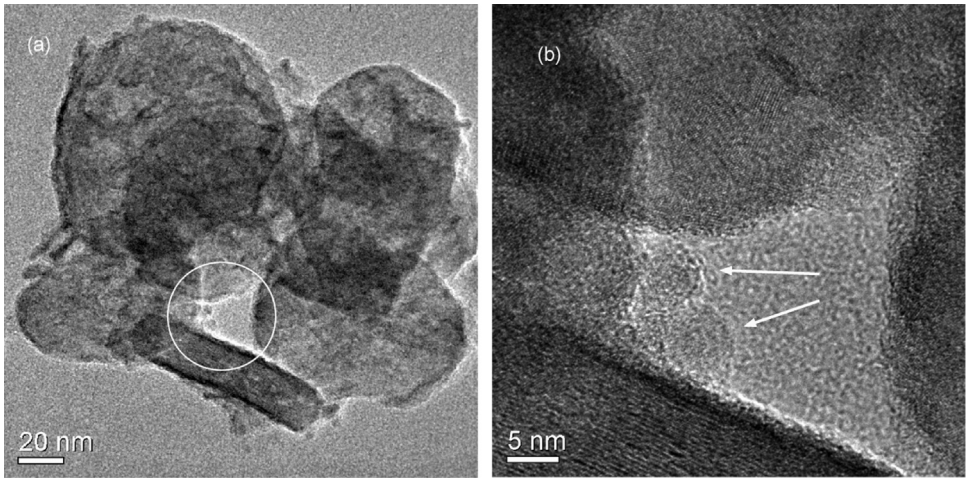

Fig. 4. (a) High resolution transmission electron microscopy of sample 08A1, where two types of morphologies can be viewed. (b) Detail of the HRTEM image showing small particles with diameter of about 5–10 nm.

spectroscopy or nuclear magnetic resonance (10^{-9}–10^{-7} s). If $\tau_m \gg \tau$ the nanoparticles are considered to be in the superparamagnetic regime, and no spontaneous magnetization is found. On the other hand, if $\tau \gg \tau_m$ the nanoparticles are in the blocked regime, and a non-zero magnetization is observed. One can obtain the critical superparamagnetic diameter for a magnetic nanoparticle using the typical measurement time for conventional magnetometry, at a certain temperature T [15]:

$$D_{cr}^{spm} \sim \left(\frac{150}{\pi}\frac{k_B T}{K}\right) \tag{1}$$

where k_B is the Boltzmann constant and K is the anisotropy.

The description of the magnetization reversal of monodomain nanoparticles has been addressed and modeled by many authors, e.g., the classical work of Stoner and Wohlfarth (SW) [17]. In cases in which the effects of temperature have to be taken into account, one can use the Bean and Livingston model [18], and for the cases where the system displays a random distribution of easy magnetization axes, one can write [19,20]

$$H_C = 0.48\frac{2K}{\mu_0 M_S}\left[1 - \left(\frac{T}{T_B}\right)^b\right], \tag{2}$$

where H_C is the coercive field, M_S is the saturation magnetization and b is an exponent that varies from 0.5, in the case of oriented particles, to 0.77 in the case of randomly oriented particles.

One can see from Eq. (2) that the blocking temperature can be extracted by measuring the magnetization as function of the applied field for different temperatures.

It is important to note that the magnetization curves show a hysteresis loop only below a certain temperature, the blocking temperature (T_B), and above this temperature the magnetization process is reversible, presenting no coercive field (H_C=0).

Using the coercive field extracted from the magnetization loops (Fig. 6) with the corresponding temperatures and fitting to Eq. (2), we obtained a blocking temperature of T_B = 12.9 K and an exponent of b=0.77 as can be viewed on the upper inset in Fig. 6 for sample 04B1.

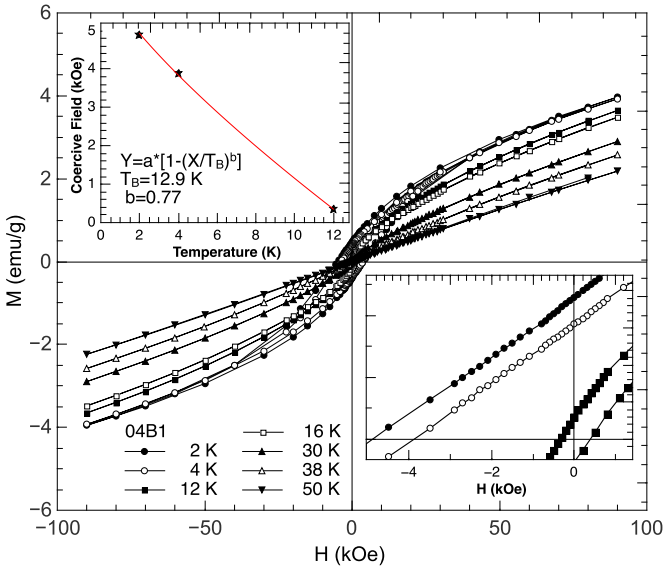

Fig. 6. Magnetization curves as function of the applied magnetic field of the sample 04B1 for different temperatures. Lower inset: Detail of the magnetization curves showing the coercive fields and magnetic remanence. Upper inset: Coercive field *versus* temperature fitting.

3.2.2. Blocking temperature from thermal cycles

An important tool for understanding the thermal dependence on the magnetization processes are the zero field-cooled (ZFC) and field-cooled (FC) protocols in which the sample is subjected to a thermal cycle in the absence or presence of a magnetic field. The protocol enables one to obtain important features of the thermally activated magnetic processes, e.g. distribution of blocking temperatures, irreversibilities, phase transitions, magnetic interactions and other parameters.

Usually, the ZFC and FC protocols are used to obtain magnetization versus temperature curves that can be divided into two regions with respect to the blocking temperature. One for $T > T_B$ and the other for $T < T_B$.

For $T > T_B$, the magnetic moments of the particles are in thermal equilibrium during the measuring time (isotropic SPM) and the magnetization follows a Langevin-like behavior.

For $T < T_B$, the nanoparticles magnetic moments are in a blocked SPM state and the magnetization will depend upon its previous magnetic history. Thus, in the blocked state, the ZFC and FC curves are different from each other, and assuming that both M_S and K dependencies with temperature can be neglected, one can write [21,22]

$$\frac{d[\chi_{FC} - \chi_{ZFC}]}{dT} = \frac{M_S^2}{3K}\left[\ln\left(\frac{\tau_m}{\tau_0}\right) - 1\right] f(T_B), \tag{3}$$

where M_S is the magnetization on the saturation, $\tau_0 \sim 10^{-9}$ s and $f(T_B)$ is the blocking temperature distribution function.

According to Eq. (3), from ZFC and FC measurements it is possible to obtain the blocking temperature distribution $f(T_B)$. Finally it is possible also to obtain a temperature value for which $\chi_{FC} - \chi_{ZFC}$ reaches its null value, the irreversibility temperature (T_{irr}), where the magnetization goes from a blocked SPM state to an isotropic one.

Figs. 7 and 8 show the ZFC, FC and (FC–ZFC) curves for a cooling field of 100 Oe, obtained for samples 04B1 and 08A1, respectively. At the first protocol (ZFC curve) the temperature is lowered until it reaches the minimum value (2 K in this case) with no applied magnetic field, leaving the magnetic moments in a blocked random state. After that step, the magnetic field is applied and the second protocol begins (FC curve) with an increment in temperature until it reaches the maximum value (300 K in this case). When the FC protocol begins, the magnetic moments that were

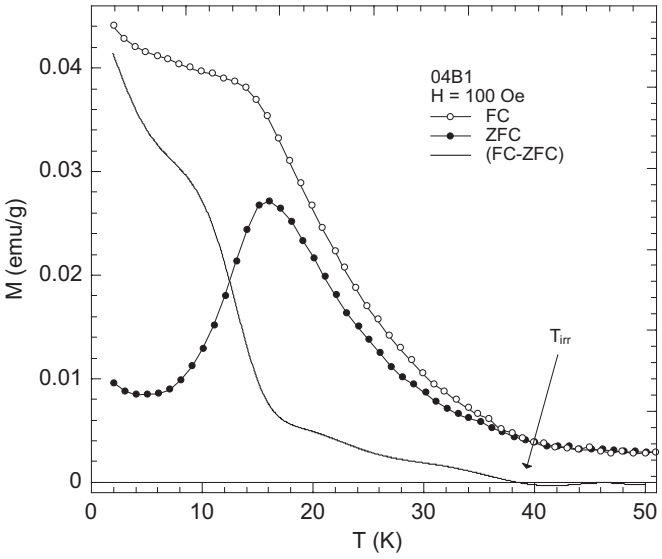

Fig. 7. ZFC, FC and (FC–ZFC) curves for sample 04B1 with a cooling field of 100 Oe. All other curves present similar behavior with clear T_B and T_{irr}.

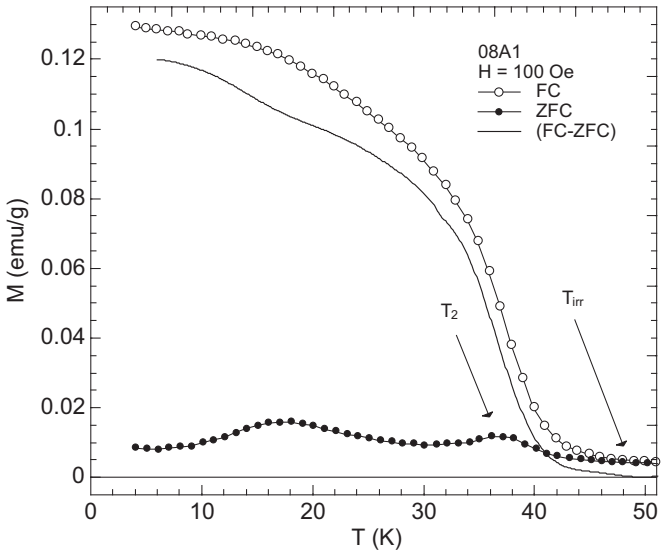

Fig. 8. ZFC, FC and (FC–ZFC) curves for sample 08A1 with a cooling field of 100 Oe. All other curves present similar behavior with clear T_B, T_2 and T_{irr}.

blocked, will unblock as they have sufficient thermal energy (k_BT) to overcome the potential barrier ($\Delta E = KV$). This process will continue until the temperature reaches T_{irr}, when the magnetization goes to an isotropic SPM state.

For both samples the unblocking process observed at low temperatures is very similar, that means both the T_B peak and T_{irr} decrease with increasing external magnetic field intensity, but for sample 08A1, the value of T_{irr} does not present a significant change. That could be an artifact caused by the influence of the second peak (T_2).

As can be seen in Fig. 8, the sample 08A1 presents two peaks in the zero field-cooled curve. This could be associated with one bimodal particle size distribution, if the two peaks change its position with an applied magnetic field.

Fig. 9 shows the derivative of the (FC–ZFC) curves, for different external magnetic fields, that is proportional to $f(T_B)$. The curves for sample 04B1 present a function with a maximum that is considered the maximum value (T_B) of the blocking temperature distribution $f(T_B)$. For the case of sample 08A1 two maxima were found in the curves, for T_B and T_2. The first one is associated with the blocking temperature distribution and the second one may be associated with a minority magnetic phase in the sample, which is in correspondence with the result obtained by X-ray diffraction. As the second peak (T_2) does not present a significant change under the action of the external magnetic field (T_2~36 K), it can be related not to an unblocking process like the first one, but to a magnetic transition (e.g., Néel-like) of the minority phase. Using X-ray profile analysis it is not possible to determine the average particle size of this minority phase, due to the very small peak/background ratio. However, due to the high bismuth volatility, one probable candidate for this minority phase is γ-Mn_2O_3. This system is ferrimagnetic, with Néel temperature of about 39 K, and has been previously reported by Kim et al. [23].

As the blocking temperature distribution is related to the $V/\langle V\rangle$ ratio, its large width suggests a particle size distribution, which is supported also by the XRD and TEM microstructural studies.

Table 1 summarizes the principal values extracted from the derivative of $M_{FC} - M_{ZFC}$ curves for different values of the applied external field.

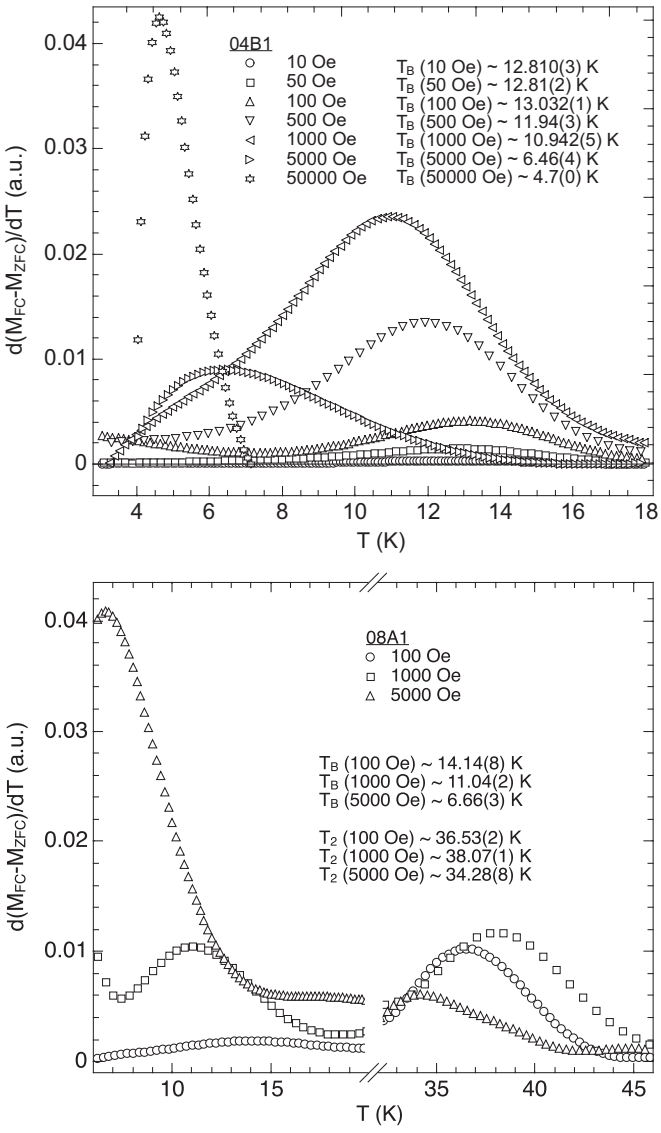

Fig. 9. Derivative of $M_{FC} - M_{ZFC}$ curves for 04B1 and 08A1 samples.

Table 1
Blocking temperature values extracted from χ_{AC}, $\frac{d[\chi_{FC} - \chi_{ZFC}]}{dT}$, and MxH curves.

Sample	Magnetic field	T_B[a]	T_B[b]	T_{irr}[b]	T_B[c]	T_2
04B1	–	–	–	–	12.9 K	–
	0 Oe	13.0 K	–	–	–	–
	10 Oe	–	12.8 K	43.0 K	–	–
	50 Oe	–	12.8 K	42.7 K	–	–
	100 Oe	–	13.1 K	42.0 K	–	–
	500 Oe	–	11.9 K	40.0 K	–	–
	1000 Oe	10.4 K	10.9 K	38.5 k	–	–
	5000 Oe	6.9 K	6.5 K	30.0 k	–	–
	50 000 Oe	–	4.7 K	11.3 K	–	–
08A1	0 Oe	13.6 K	–	–	–	–
	100 Oe	–	14.1 K	53.0 K	–	36.5 K
	1000 Oe	11.3 K	11.0 K	53.0 K	–	38.1 K
	5000 Oe	7.1 K	6.7 K	57.0 K	–	34.3 K

[a] From AC susceptibility.
[b] From thermal cycles.
[c] From magnetization loops.

3.2.3. Blocking temperature from AC susceptibility: anisotropic superparamagnetism

We will now consider the situation in which $k_BT > KV$. Here, the nanoparticle's magnetization has sufficient thermal energy to overcome the anisotropy energy barrier (KV) and change its magnetization direction, although not by a free rotation, because

of the finite width of the potential well. Therefore the magnetization direction can fluctuate between two possible energy minima with frequency f, or a characteristic relaxation time $\tau = 1/f$ given by the Néel–Brown equation [24]:

$$\tau = \tau_0 \exp\left(\frac{KV}{k_B T}\right) \tag{4}$$

This fluctuation becomes slower (τ becomes larger) when the system is brought to low temperatures.

An AC susceptibilty study of the characteristic relaxation times of this system has been addressed by de Oliveira et al. [8] and it was found that although the system follows an Arrhenius law, it has an unusual relaxation time.

The system appears to be static when the SPM relaxation time, τ, turns out to be much greater than the experimental measuring time, τ_m. When $\tau < \tau_m$ one can observe an average value for the magnetization, and when τ is comparable to τ_m, the particle is said to be blocked. Manipulating Eq. (4), we obtain

$$T_B \sim \frac{KV}{k_B} \ln\left(\frac{\tau_m}{\tau_0}\right)^{-1} \tag{5}$$

where T_B is the blocking temperature. Eq. (5) is valid for the individual particles or to a system of non-interacting particles with the same size and anisotropy. In a non-monodisperse system, the size distribution will result in a distribution of blocking temperatures.

AC magnetic susceptibility measurements were performed as a function of temperature with an applied AC magnetic field of 10 Oe and frequencies varying from 100 to 10 kHz, plus DC magnetic fields of 0, 1 and 5 kOe. Fig. 10 presents the real (χ') and imaginary (χ'') components of the AC magnetic susceptibility (χ_{AC}), measured for a DC magnetic field of 1 kOe. As the AC frequency value increases, the peak position changes to higher values of temperatures, both for χ' and χ''.

The blocking temperature values, extracted from the AC susceptibility measurements, were obtained with the help of Eq. (5) by linearizing Eq. (4), taking the logarithm on both sides, where KV/k_B and τ_0 were obtained from the linear fit and for $\tau_m = 100$ s. These values are summarized in Table 1 for different values of the DC applied magnetic field.

The presence of the DC magnetic field, while the AC susceptibility is measured, affects the double well potential that governs the magnetic relaxation of the system [17]. Therefore, the blocking temperatures are expected to be field dependent as the system will need less thermal energy to unblock.

There are several terms in a magnetic material that can effectively contribute to its total anisotropy (e.g. crystalline, shape, surface, stress, Néel, etc.) [25]. In simple cases, one can write the total anisotropy energy density in terms of an effective anisotropy constant K_{eff}, as:

$$\frac{E_A}{V} = K_{eff} \sin^2 \theta, \tag{6}$$

where the range in magnitude of the anisotropy energy in magnetic materials is $\pm(10^2–10^7)$ J m^{-3} [15].

Using the blocking temperature value for zero applied magnetic field, 13.0 K and 13.6 K, and the average nanoparticle size from DRX and TEM data, 43 nm and 22 nm, with the aid of Eq. (1), one can calculate the effective anisotropy constant (K_{eff}) of this material, that was found to be $K_{eff} \sim 1 \times 10^2$ J m^{-3} and $K_{eff} \sim 9 \times 10^2$ J m^{-3} for samples 04B1 and 08A1, respectively.

4. Conclusions

In conclusion, manganese sillenite ($Bi_{12}MnO_{20}$) superparamagnetic nanoparticles were synthesized by a low temperature soft chemical route under refluxing conditions, and their structure, microstructure and a complete and comparative study of the thermal activated processes were explored.

From the XRD analysis and Williamson–Hall method for deconvoluting size and strain contributions to line broadening, we conclude that we are dealing with a distribution of particle sizes of

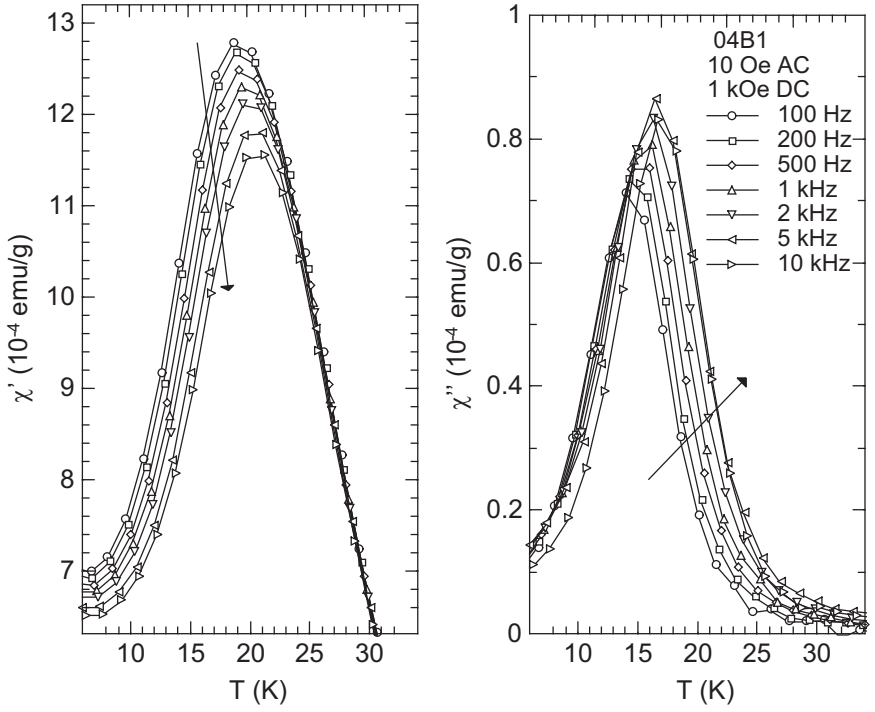

Fig. 10. Temperature dependence of the in-phase, $\chi'(T)$, and out-of-phase, $\chi''(T)$ components of the magnetic susceptibility for the 04B1 sample for different frequency values (100, 200, 500, 1 k, 2 k, 5 k, and 10 kHz), where the arrows indicate the increase in frequency.

43 nm (04B1) and 22 nm (08A1). The sample 08A1 also presents a small particle size distribution (5–10 nm), observed with HRTEM, that is responsible for the increased background at the bottom of the most intense diffraction peaks.

The magnetization curves show hysteresis for temperatures below the blocking temperature that, by fitting with the modified Bean–Livingstone model, was found to be $T_B = 12.9$ K, with an exponent of $b = 0.77$ for the 04B1 sample.

The thermal dependence on the magnetization processes was studied with the zero-field-cooled and field-cooled protocol. The sample 04B1 shows a classical superparamagnetic nanoparticle behavior with a maximum on the ZFC curves related to the blocking temperature, followed by an irreversible temperature, were the system goes from a SPM blocked state to an isotropic one with a Langevin-like behavior. For the lowest applied field (10 Oe) the sample 04B1 presented a blocking temperature of $T_B \sim 12.8$ K. The sample 08A1 presents two maxima on the ZFC curves, the first one related to the blocking temperature and the second to a magnetic transition of the possible minority phase γ-Mn_2O_3 ($T_N \sim 36$ K). All these results show a blocking temperature that is field dependent.

AC susceptibility measurements for different values of the DC applied magnetic field confirm that the blocking temperature is field dependent, as expected for SPM systems. The blocking temperatures obtained for samples 04B1 and 08A1 were $T_B \sim 13.0$ K and $T_B \sim 13.6$ K, respectively.

The three different techniques used to obtain the $Bi_{12}MnO_{20}$ blocking temperature show that this system displays an isotropic superparamagnetic behavior with a blocked state for temperatures below 13 K. All the techniques yield approximately the same blocking temperature values and their applied magnetic field dependence.

Acknowledgments

The authors would like to thank the Brazilian agencies CNPq (Grants 305667/2014-9 and 308798/2009-0), FAPERJ (Grants E26/010.002996/2014 and E-26/102.738/2008) and CAPES (Grant CAPES/MESCUBA 310/2012) for financial support. The authors would like to thank LNLS and LNNano in Campinas Brazil for the synchrotron and electron microscopy experiments in the framework of the projects XPD-9296, XPD-10698, Inspect-14929, Inspect-14958.

References

[1] E.M. Levin, R.S. Roth, J. Res. Natl. Bur. Stand. Sec. A A68 (1964) 197–206.
[2] M. Zaleski, J. Appl. Phys. 87 (9, Part 1) (2000) 4279–4284.
[3] E. Nippolainen, A.A. Kamshilin, V.V. Prokofiev, T. Jaaskelainen, Appl. Phys. Lett. 78 (7) (2001) 859–861.
[4] M. Valant, D. Suvorov, J. Am. Ceram. Soc. 84 (12) (2001) 2900–2904.
[5] M. Valant, D. Suvorov, J. Am. Ceram. Soc. 85 (2) (2002) 355–358.
[6] S. Chehab, P. Conflant, M. Drache, Boivin, Mater. Res. Bull. 38 (5) (2003) 875–897.
[7] S.C. Abrahams, P.B. Jamieson, J.L. Bernstei, J. Chem. Phys. 47 (10) (1967) 4034.
[8] L.A.S. de Oliveira, J.P. Sinnecker, M.D. Vieira, A. Penton-Madrigal, J. Appl. Phys. 107 (9) (2010).
[9] J.L. Fourquet, A. Lebail, P.A. Gillet, Mater. Res. Bull. 23 (8) (1988) 1163–1170.
[10] J. Rodriguez Carvajal, Technical Report, CEA-CNRS, Saclay, France, 1990.
[11] G.K. Williamson, W.H. Hall, Acta Metall. 1 (1) (1953) 22–31.
[12] J. Frenkel, J. Dorfman, Nature 126 (1930) 274.
[13] R.C. O'Handley, Modern Magnetic Materials: Principles and Applications, Wiley-VCH, Weinhein, 2000.
[14] J.M.D. Coey, Magnetism and Magnetic Materials, Cambridge, United Kingdom, 2009.
[15] A.P. Guimaraes, Principles of Nanomagnetism, Springer-Verlag, Berlin, Heidelberg, 2009.
[16] M. Knobel, W.C. Nunes, L.M. Socolovsky, E. De Biasi, J.M. Vargas, J.C. Denardin, J. Nanosci. Nanotechnol. (8) (2008) 2836–2857.
[17] E.C. Stoner, E.P. Wohlfarth, Philos. Trans. R. Soc. A 240 (1948) 599–642.
[18] C.P. Bean, J.D. Livingston, J. Appl. Phys. 30 (4) (1959) 120S–129S.
[19] H. Pfeiffer, Phys. Status Solidi A (120) (1990) 233.
[20] J. Garcia-Otero, A.J. Garcia-Bastida, J. Rivas, J. Magn. Magn. Mater. 189 (3) (1998) 377–383.
[21] H. Mamiya, M. Ohnuma, I. Nakatani, T. Furubayashim, IEEE Trans. Magn. 41 (10) (2005) 3394–3396.
[22] L.G. Paterno, F.J. Fonseca, G.B. Alcantara, M.A.G. Soler, P.C. Morais, J.P. Sinnecker, M.A. Novak, E.C.D. Lima, F.L. Leite, L.H.C. Mattoso, Thin Solid Films 517 (5) (2009) 1753–1758.
[23] S.H. Kim, B.J. Choi, G.H. Lee, S.J. Oh, B. Kim, H.C. Choi, J. Park, Y. Chang, J. Korean Phys. Soc. 46 (4) (2005) 941–944.
[24] L. Néel, Ann. Geophys. 5 (1949) 99–136.
[25] A.P. Guimaraes, Magnetism and Magnetic Resonance in Solids, Wiley, New York, 1998.